Shedding light on CO oxidation surface chemistry on single Pt catalyst nanoparticles inside a nanofluidic model pore

ACS Catalysis

pubs.acs.org/acscatalysis

Research Article

Shedding Light on CO Oxidation Surface Chemistry on Single Pt Catalyst Nanoparticles Inside a Nanofluidic Model Pore

David Albinsson, Stephan Bartling, Sara Nilsson, Henrik Ström, Joachim Fritzsche, and Christoph Langhammer*

Cite This: *ACS Catal.* 2021, 11, 2021−2033

Read Online

ACCESS | Metrics & More | Article Recommendations | Supporting Information

ABSTRACT: Investigating a catalyst under relevant application conditions is experimentally challenging and parameters like reaction conditions in terms of temperature, pressure, and reactant mixing ratios, as well as catalyst design, may significantly impact the obtained experimental results. For Pt catalysts widely used for the oxidation of carbon monoxide, there is keen debate on the oxidation state of the surface at high temperatures and at/above atmospheric pressure, as well as on the most active surface state under these conditions. Here, we employ a nanoreactor in combination with single-particle plasmonic nanospectroscopy to investigate individual Pt catalyst nanoparticles localized inside a nanofluidic model pore during carbon monoxide oxidation at 2 bar in the 450−550 K temperature range. As a main finding, we demonstrate that our single-particle measurements effectively resolve a kinetic phase transition during the reaction and that each individual particle has a unique response. Based on spatially resolved measurements, we furthermore observe how reactant concentration gradients formed due to conversion inside the model pore give rise to position-dependent kinetic phase transitions of the individual particles. Finally, employing extensive electrodynamics simulations, we unravel the surface chemistry of the individual Pt nanoparticles as a function of reactant composition and find strongly temperature-dependent Pt-oxide formation and oxygen spillover to the SiO_2 support as the main processes. These results therefore support the existence of a Pt surface oxide in the regime of high catalyst activity and demonstrate the possibility to use plasmonic nanospectroscopy in combination with nanofluidics as a tool for in situ studies of individual catalyst particles.

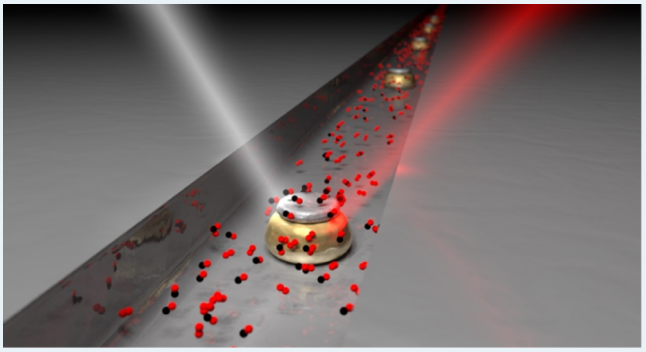

KEYWORDS: *single particle, CO oxidation, plasmonic, platinum, nanoreactor, nanofluidics, in situ*

INTRODUCTION

Kinetic bistability is a characteristic property of the carbon monoxide (CO) oxidation reaction and the consequence of the poisoning effect that CO has on catalysts due to its strong bond with Pt-group metals.[1−5] This effect is responsible for the so-called cold-start problem of three-way catalytic converters. Mechanistically, it has been shown to be strongly influenced by changes in the apparent rate coefficients of the elementary reaction steps, which in turn are controlled by the given reaction conditions in terms of the pressure, temperature, and relative reactant concentration (α^{CO}), as well as by the catalyst design.[6] Here, α^{CO} is defined as

$$\alpha^{CO} = \frac{C_{CO}}{C_{CO} + C_{O2}} \quad (1)$$

where α^{CO} is the relative CO concentration and c_i is the gas-phase concentration of species i. The existence of two separate kinetic phases is caused by the fact that the catalyst either can find itself in a state of low activity, when the surface is CO poisoned, or in a highly active state, where its surface is predominantly covered by dissociated chemisorbed oxygen (O). Bistability arises when both states can be kinetically stable for the same reactant mixing ratio. This occurs in the low-temperature regime, where the state depends on the previous state of the catalyst in terms of α^{CO}, giving rise to hysteresis.[3,5] In the O-dominated regime, the reaction rate is almost proportional to the supplied CO concentration, since the influence of O on the adsorption probability of CO is small, and it increases until a critical relative CO concentration, α^*, is reached, and a so-called kinetic phase transition[7] to a new state takes place. In this new state, CO predominantly covers the surface and the reaction rate is reduced because the adsorbed CO molecules effectively block chemisorption of O_2 and thus

Received: November 13, 2020
Revised: January 20, 2021
Published: February 1, 2021

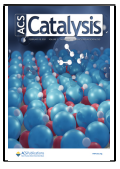

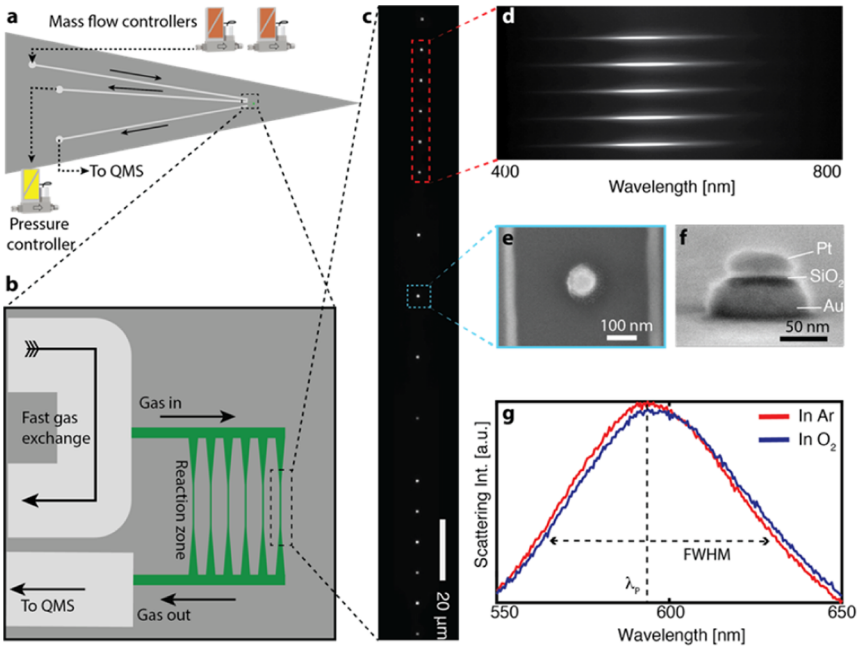

Figure 1. Nanoreactor chip design. (a) Schematic layout of the nanofluidic chip with inlet and outlet μ-channels that connect the nanoreactor to the gas supply system. (b) Reaction zone of the chip where the nanofluidic reactor consists of six parallel nanofluidic channels—the model pores—each containing catalyst nanoparticles. (c) Optical microscope image of a nanofluidic model pore containing 16 nanoparticles. (d) Spectroscopic CCD image of five individual catalyst nanoparticles inside the model pore. (e) Scanning electron microscopy (SEM) micrograph of a particle placed inside a ca. 400 nm wide nanofluidic model pore. (f) Side-view SEM image of a representative Au−SiO_2−Pt hybrid nanoparticle consisting of a 40 nm high Au base covered by an 8 nm thick SiO_2 layer with a 15 nm thick Pt catalyst on top. The image was taken after annealing at 823 K in N_2 for 12 h. (g) Scattering spectra of such a hybrid nanostructure at 523 K in pure Ar flow (red) and in 7% O_2 in Ar (blue). The spectral position of the localized surface plasmon resonance (LSPR) peak maximum (λ_P) and the full width at half-maximum (FWHM) are indicated by the dashed lines.

limit the supply of O to form CO_2. When decreasing α^{CO}, a similar scenario takes place but with the kinetic phase transition at different α^* due to hysteresis.[3,5,7]

In this context, there is also ongoing debate about the most active phase of Pt under application conditions, where the exact role of a formed surface oxide layer is still not fully established.[8−14] This is, to a large extent, the consequence of the fact that most insights related to CO oxidation over Pt catalysts over the last decades have been generated on the basis of surface science studies on (single crystal) model catalysts at low pressures, where no significant surface oxide formation has been observed.[1,3,15] More recently, structurally less perfect systems have been investigated and studies under more technologically relevant conditions in terms of pressure have become available. To this end, it has been shown for polycrystalline Pt foils under low-pressure conditions that α^* exhibits a distinct dependence on the surface index of the individual crystallites in the foil[3] and that the abundance of different facets and defects influences the nature of the bistability.[5,16] Furthermore, studies performed at higher pressures have indicated more dramatic changes in the Pt surface during CO oxidation.[12,17] One study, performed at 0.5 bar, investigated Pt(110) with surface-sensitive X-ray diffraction (XRD) and concluded that an oxide surface had significantly higher activity than a metallic Pt-terminated surface.[8] Similarly, time-resolved X-ray absorption spectroscopy (XAS) of a packed-bed reactor investigated at atmospheric pressure and 382 K has, with millimeter spatial resolution, identified the mechanism of oscillations in CO oxidation as mediated by the local transient formation of a highly disordered Pt oxide.[9] In contrast, another operando XAS and IR thermography study, conducted at atmospheric pressure and 373−448 K, concluded that reduced Pt was responsible for the highest activity and that Pt-oxide formation resulted in reduced activity.[10] Similarly, ambient-pressure X-ray photoelectron spectroscopy (AP-XPS) at 250 mTorr was used to study Pt(110) during CO oxidation and an α-PtO_2 phase was detected as a less active phase than an oxygen-terminated Pt surface.[11] Furthermore, in situ transmission electron microscopy (TEM) studies have revealed that the chemical dynamics on Pt nanoparticles are mediated both by morphological transformations and by structural changes.[2,18,19] Finally, we have recently demonstrated that the kinetic phase transition can be resolved on single Pt nanoparticles using plasmonic nanospectroscopy at atmospheric pressure.[20] However, to the best of our knowledge, no studies exist that investigate the surface oxidation state and the CO oxidation reaction kinetics of a Pt nanocatalyst under high-pressure conditions with single nanoparticle resolution and for a catalyst material that takes the distribution of the metal nanoparticles in a nanoconfined space explicitly into account. The former is, however, critical if ensemble averaging is to be avoided to enable a direct quantitative comparison of experiments with theoretical modeling. The latter is important because the nanoconfinement may locally define reaction conditions that are very different from the global ones. In other words, the catalyst may locally attain different oxidation states or experience significantly different reactant compositions at different positions, e.g., due to local conversion on neighboring particles in direct proximity, or generally due to reactant conversion on particles upstream.[21]

https://dx.doi.org/10.1021/acscatal.0c04955
ACS Catal. 2021, 11, 2021−2033

Here, we set out to investigate the impact of single Pt nanoparticle morphology, Pt-oxide formation, and oxygen (O) spillover on the CO oxidation reaction kinetics under high-pressure conditions, as well as to highlight the ramifications of nanoconfinement in the single nanoparticle spatial position along a nanofluidic model pore, using a newly developed nanoreactor platform.[21] It capitalizes on the assets of nanofluidics, single-particle plasmonics, finite-difference time-domain (FDTD) electrodynamics simulations, and online mass spectrometry, to enable the scrutiny of catalyst surface state and reactant transport and conversion effects at the individual nanoparticle level and under reaction conditions at 2 bar total pressure. Furthermore, our solution enables the direct comparison between optical single-particle spectroscopy response and the simultaneously measured catalytic activity, acquired from an ensemble with a well-controlled population of ca. 3×10^4 nanoparticles with the same dimensions. This ensures that the obtained single-particle results can be directly benchmarked and discussed with respect to a statistically relevant ensemble, as it would be present in a technical application of the catalyst.

RESULTS

Nanofluidic Reactor. By utilizing our recently introduced nanoreactor platform,[21] we are able to perform operando catalyst characterization on ultrasmall samples under continuous flow conditions. The platform comprises a nanofluidic chip (Figure 1a) that is connected via a sample holder to a stainless-steel gas handling system, a quadrupole mass spectrometer (QMS), and a power controller for the on-chip heater enabling operation at up to 723 K. This nanoreactor is then mounted on an upright optical microscope connected to a spectrometer equipped with an electron multiplying charge coupled device (EM-CCD) camera that facilitates simultaneous single-particle plasmonic nanospectroscopy[22] from up to 18 catalyst particles located inside a nanofluidic channel, which we call the model pore (Figures 1b–d and S1, and further details in ref 21).

Plasmonic nanospectroscopy is based on the localized surface plasmon resonance (LSPR) phenomenon, which occurs upon interaction of light with metallic nanoparticles smaller than the wavelength.[23] It induces collective and coherent resonant oscillations of the electrons in the particles, which results in a strong interaction with the incoming light that is reflected in a distinct peak in the scattering and absorption spectra. Since the LSP frequency is dictated by particle properties like size, shape, and composition, as well as the surrounding medium, plasmonic metal nanoparticles are excellent probes of nanoscale processes that occur directly on their surfaces or in their close vicinity, both at the ensemble and single nanoparticle levels.[20,21,24−28]

The nanoreactor chip itself is micro- and nanofabricated in a thermally oxidized silicon wafer, as described in detail in the Methods section and Figure S2. It is comprised of a microfluidic inlet and outlet system that connects to a sample holder toward the high-pressure gas supply (inlet) side and the low-pressure QMS side (Figure 1a,b). The U-design at the inlet (Figure 1b) serves the purpose of enabling fast gas exchange using conventional mass flow controllers. On the other end, the microfluidic system connects to the nanofluidic system comprising six identical nanofluidic channels that form the actual model pores (Figure 1b). Each channel is 600 μm long and designed as symmetric funnel that narrows down to a center region that is 100 μm long, has a width of 400 nm, and a height of 100 nm. The model pores are decorated with catalyst nanoparticles comprised of Au−SiO_2−Pt hybrid nanostructures, where a bottom Au nanoantenna acts as an inert plasmonic probe of the adjacent 70 nm × 15 nm Pt catalyst disk,[20,25] separated by an 8 nm thick SiO_2 support layer (Figure 1e,f). Transmission electron microscopy (TEM—Figure 2a–f) and reflection high-energy electron diffraction

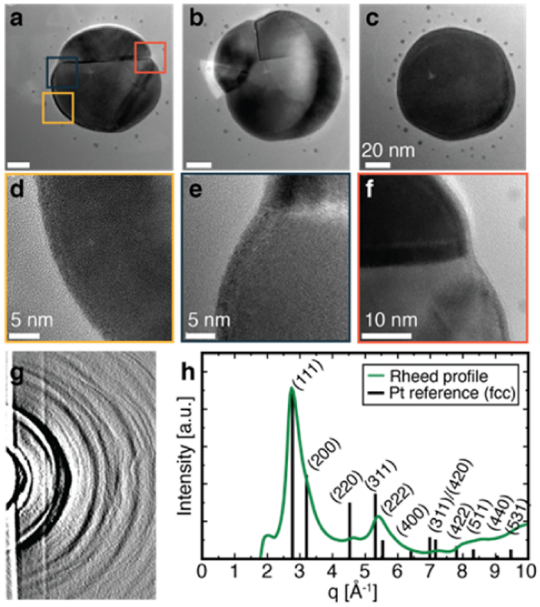

Figure 2. Characterization of Pt catalyst nanoparticles. (a–c) TEM images of three representative Pt particles (prepared on a TEM membrane and without a Au nanoantenna underneath to enable imaging) revealing their polycrystalline nature, as well as the difference in the abundance of grains and high-angle grain boundaries, and thus types/abundance of facets and low-coordination defect sites. (d–f) High-resolution TEM images corresponding to the colored squares in (a). (g, h) Reflection high-energy electron diffraction (RHEED) measurement on a Pt nanoparticle sample analogue treated in 9% CO and 9% O_2 diluted in Ar at 623 K for 1 h in each gas mixture. (g) The averaged diffraction pattern consists of pronounced ring features (high intensity is shown dark shade; for suppression of slowly varying background, the Laplace operator is applied), indicating polycrystalline three-dimensional (3D) structures on the surface. (h) The radial intensity profile (green) reveals clear peaks, which correspond to Pt with an face-centered cubic (fcc) crystal structure. The vertical black lines indicate the calculated positions and relative intensities for fcc Pt.

(RHEED—Figure 2g,h) of Pt nanoparticle analogues without an adjacent Au nanoantenna reveal that the Pt particles are polycrystalline with multiple grains, distinct high-angle grain boundaries, and different grain orientations. In the TEM micrographs (Figure 2a–f), we also notice some small particles (satellites) surrounding the larger main particle. Such satellites are often observed for electron beam-evaporated nanostructures. Even though they also are catalytically active, their contribution to the total activity measured in our experiment is likely negligible due to their relatively small surface area compared to the large disks that are tracked in the optical experiments.

In the model pore considered here, the individual catalyst nanoparticles were placed by means of electron beam lithography during nanofabrication with a particle separation

https://dx.doi.org/10.1021/acscatal.0c04955
ACS Catal. 2021, 11, 2021−2033

of 10 μm in the funnels and 20 μm in the narrow central region. The particles appear as individual, separated point sources through the dark-field microscope (Figure 1c) equipped with an aperture to suppress scattering from the channel walls.[29] Furthermore, in the other channels, high-density arrays of catalyst particles were fabricated (Figure S3), such that a total of 3×10^4 nanoparticles of the same size are present on the chip. These separate additional nanochannels serve the purpose of ensuring that the QMS response is obtained from a total particle number that is large enough to constitute a statistically relevant ensemble, which allows the important direct comparison between the single-particle response obtained by plasmonic nanospectroscopy from the single nanoparticles and the corresponding ensemble response in one and the same experiment.

CO Oxidation Experiments. Catalytic CO oxidation experiments were conducted by introducing a mixture of CO and O_2 in Ar carrier gas and varying α^{CO} in the reactant flow from CO-rich (high α^{CO}) to O_2-rich (low α^{CO}) conditions and back while keeping the total reactant concentration constant at 7% (Figure 3a). In a first experiment, the reaction conditions were fixed at a reactor temperature of 503 K and an inlet pressure of 4 bar. This results in a pressure of ca. 2 bar at the catalyst position in the model pore (Figure S4).[21] During two consecutive identical sweeps, we simultaneously recorded the main reaction product CO_2 (Figure 3b) and the optical scattering spectra from the catalyst nanoparticles in the model pore, and we used the change in full width at half-maximum (ΔFWHM) of the plasmonic scattering peak as the main readout (Figure 3c). We chose ΔFWHM because it is less sensitive to drift and vibrations of the sample during the up to 24 h long experiments, compared to the more traditionally used measurements of the spectral shift of the plasmonic scattering peak, $\Delta\lambda_p$ (Figure S5). However, comparing the evolution of both these parameters in combination with finite-difference time-domain (FDTD) simulations can provide mechanistic insights into the chemical origin of the optical response and thus the catalyst surface state, as we discuss in detail further below.

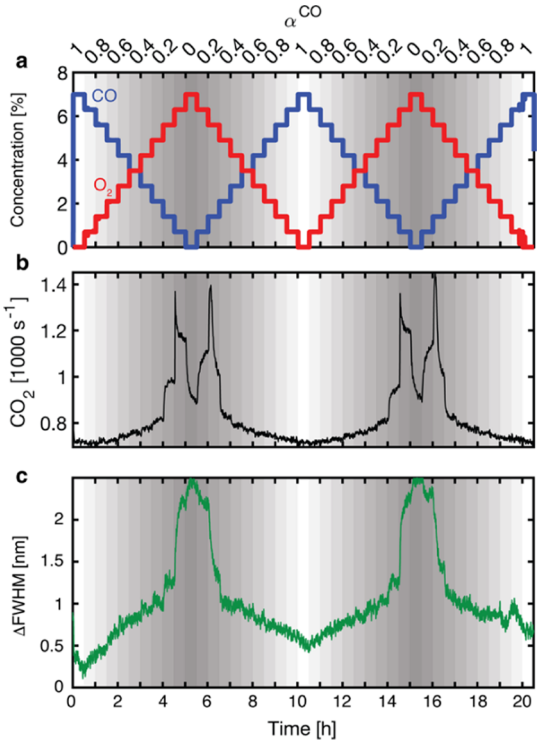

Figure 3. CO oxidation experiment. (a) Nominal global CO and O_2 concentrations in Ar carrier gas during two subsequent α^{CO} sweeps. The corresponding $\alpha^{CO} = \frac{C_{CO}}{C_{CO}+C_{O2}}$ values are presented on the top x-axis. (b) CO_2 production rate measured by the QMS for an experiment at 503 K and ~2 bar pressure in the model pore. (c) Corresponding ΔFWHM signal measured for a single Pt nanoparticle using the plasmonic nanospectroscopy readout. We notice the distinct stepwise change in ΔFWHM that coincides with the highest reaction rate measured by the QMS for both α^{CO} up and down sweeps.

As the key feature here, we observe a reversible trend of increasing ΔFWHM for decreasing α^{CO} and at least one distinct upward or downward step in ΔFWHM in the range of $\alpha^{CO} \approx 0.2$ (Figure 3c). Comparing this optical single-particle response with the simultaneously recorded rate of CO_2 formation obtained by the QMS, we find the maximum rate at $\alpha^{CO} = 0.2$, both for the up and down sweeps (Figure 3b; see Figure S6 for negative control without Pt). Based on these observations, and in agreement with previous work,[20,25] we assign the optical response to chemical transformation on the particles that are induced by the kinetic phase transition.

Having established this general understanding of our experiment, we carried out similar measurements with smaller α^{CO} steps and at temperatures ranging from 453 to 550 K (Figure 4). Focusing first on the QMS response (Figure 4a,b), we find that increasing the temperature results in the expected increased activity (Figure S7a) and a gradual shift of the reaction rate maximum to higher α^{CO} values. Furthermore, as is characteristic for the CO oxidation reaction, we observe a first-order dependence of the reaction rate on CO concentration in the O-rich regime (small α^{CO}) and a negative-order dependence on CO concentration in the CO-rich regime (large α^{CO}).[30] At the two lowest temperatures (453, 473 K), we observe hysteresis between the up and down sweeps in α^{CO} (Figure 4b), while no hysteresis is observed at temperatures above 473 K. This is in good agreement with an increasing CO desorption rate that eliminates the poisoning effect and thus terminates the bistability of the reaction.[5,7]

Turning to the optical response from the single nanoparticle, we consistently see the occurrence of a large change in FWHM close to the α^{CO} region with the highest reaction rate for all temperatures (Figure 4c,d). With increasing temperature, the region of high activity widens (Figure 4a,b) and the corresponding optical response occurs over a wider α^{CO} range as well (Figure 4c,d). Thus, the corresponding transition from a predominantly CO-covered to a predominantly O-covered catalyst surface region extends over a broader α^{CO} range as the temperature is increased. Increasing the temperature also results in a larger absolute optical response (i.e., larger ΔFWHM as well as $\Delta\lambda_{peak}$—Figure S7b), and exposing the catalyst to pure CO and O_2 prior to the α-sweep reveals that the observed optical signal is related to oxygen exposure, while exposure to CO alone results in negligible optical response (Figure S8).

To correlate the locally measured single-particle information with the globally measured activity, we extract critical α values (α^*), defined for the QMS measurement as the point where the maximum CO_2 production was observed in Figure 4a, and for the plasmonic nanospectroscopy readout as the point where $\Delta FWHM(\alpha^{CO})$ is 60% of its maximal total value for the

https://dx.doi.org/10.1021/acscatal.0c04955
ACS Catal. 2021, 11, 2021−2033

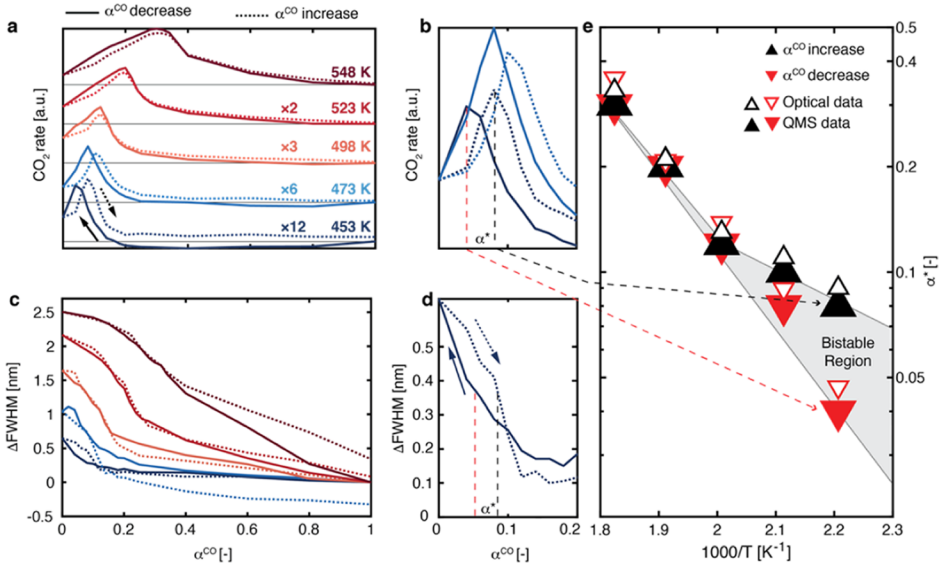

Figure 4. Temperature-dependent kinetic phase transition and kinetic bistability on a single Pt catalyst nanoparticle. (a) CO_2 production in the nanoreactor as a function of nominal inlet α^{CO} for five temperatures in the range 453−548 K. Each line has been scaled by a temperature-dependent scaling factor (indicated) to emphasize the line shapes. (b) Zoom-in of the 453 K and 473 K traces in (a). (c) Optical ΔFWHM response from a single Pt nanoparticle vs α^{CO}. (d) Zoom-in of the 453 K trace in (a). (e) Critical α^* extracted from (a) and (c) plotted vs inverse temperature. Filled triangles correspond to the QMS data and open triangles correspond to the optical ΔFWHM response. As the temperature is decreased, hysteresis appears in both readouts. The gray shaded region indicates the bistability region. The α^*-value is defined as the maximum CO_2 production rate in (a,b) and the point where ΔFWHM is equal to 60% of the total ΔFWHM at each temperature in (c, d), illustrated by dotted vertical lines in (b,d), respectively. The upward- and downward-pointing arrows indicate the directions of the α^{CO} sweep.

current temperature (i.e., the point where $\Delta\text{FWHM}(\alpha^{CO}) = 0.6 \times \max(\Delta\text{FWHM}(\alpha^{CO}))$). The reason for choosing 60% is that at this point, the ΔFWHM curve coincides with the highest reaction rate determined by the QMS. The corresponding α^* values plotted vs inverse temperature in Figure 4e then illustrate the correlation between the global QMS and local plasmonic nanospectroscopy measurements, and both confirm the existence of a region of kinetic bistability for temperatures below 500 K. However, we highlight that the two methods used resolve the bistability mechanistically in different ways. The QMS measures the formation of the reaction product and thus provides only indirect information about the reaction dynamics on the catalyst surface, whereas the plasmonic nanospectroscopy signal is directly related to the chemical processes on, and in the close surroundings of, the individual catalyst nanoparticle. For example, we note that the magnitude of the ΔFWHM shift increases with temperature, indicating that a larger chemical or structural change occurs during the reaction, as discussed in further detail below. Also, analyzing the optical response from all of the single particles in the nanofluidic model pore probed simultaneously during a sweep from high to low α^{CO} values reveals that all particles share the same general trends in their optical response (Figure 5). To enable comparisons between measurements performed at different temperatures, all data in Figure 5 are normalized by multiplying the particle- and temperature-specific $\Delta\text{FWHM}(\alpha^{CO})$ traces by $\frac{1}{\max(\Delta\text{FWHM}(\alpha^{CO}))}$. This reveals that all particles exhibit a shift of α^* toward higher α^{CO} for increasing temperatures, the presence of a kinetic phase transition in the region of the highest catalyst activity determined by the QMS, and a distinctly higher ΔFWHM level in the oxygen-covered surface regime at low α^{CO} compared to the CO-covered surface regime at high α^{CO}. At the same time distinct individuality in their response becomes apparent and can be attributed to morphological differences, such as abundance of grain boundaries and combinations of surface facets (cf. Figure 2) that exhibit kinetic phase transitions at different nominal α^{CO} values.[3] To this end, we also note that certain particle-specific behavior is reproducible over multiple CO sweeps (Figure S9), hinting at the importance of single-particle morphology (cf. Figure 2) for the kinetic phase transition process, in good agreement with a recent study on Pt and Pd foils[3] and mediated by the communication between neighboring facets via surface diffusion.[31]

Impact of Single-Particle Position Along the Model Pore. To investigate the impact of potential reactant concentration gradients inside the nanofluidic model pore, as we have observed in a previous study for a Cu catalyst,[21] we extract the α^{CO} at the kinetic phase transition (α^*) for all measured single particles (Figure 6a). Based on the stoichiometry of the reaction ($CO + 1/2O_2 \rightarrow CO_2$), the local α^{CO} is expected to decrease along the model pore due to reactant conversion, once it becomes high enough to significantly alter the nominal reactant composition. As a consequence, the α^* at the kinetic phase transition is expected to increase along the model pore since it is based on the inlet concentrations of CO and O_2. In other words, to locally reach α^* resulting in the kinetic phase transition further downstream, the nominal (inlet) α^{CO} has to be higher. Accordingly, we analyze the position dependence of α^* by plotting the optical ΔFWHM response from all nanoparticles in the model pore as a function of the nominal α^{CO} together with the QMS response for all five temperatures (Figure 6b−f). For the experiments performed at 453, 473, and 498 K, we find a weakly negative dependence of α^* as a function of position along the pore, i.e., that the kinetic phase transition occurs at lower nominal α^{CO}. In contrast, for the two highest temperatures, we observe a distinct positive trend (Figure 6g using ΔFWHM and Figure S10 using $\Delta\lambda_p$ as the optical readout), indicating that the

https://dx.doi.org/10.1021/acscatal.0c04955
ACS Catal. 2021, 11, 2021−2033

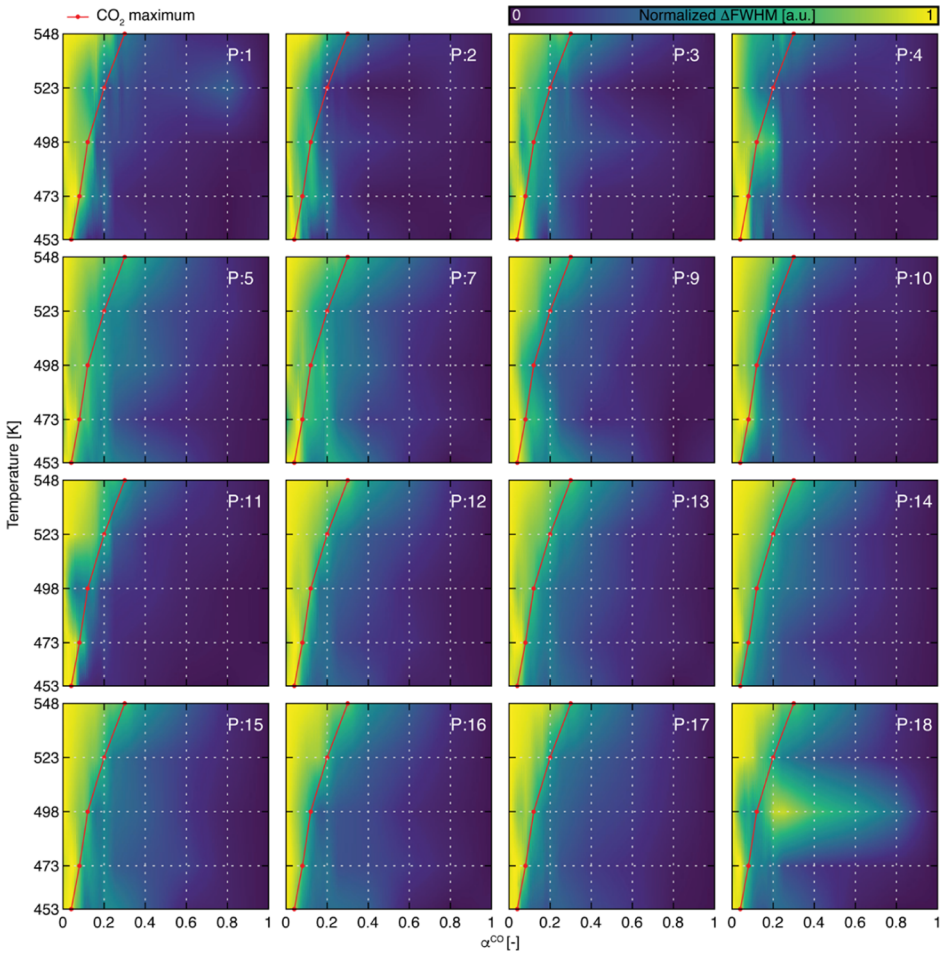

Figure 5. Plasmonic nanospectroscopy of single Pt catalyst nanoparticles. Normalized ΔFWHM (details in methods) for 16 individual particles during an α^{CO} down sweep from 1 to 0 in the temperature interval 453−548 K. The plots are interpolated from measurements performed at five temperatures indicated by the ticks on the *y*-axis. The red line corresponds to the α^{CO}-value at which the maximum CO_2 production is measured by the QMS for each temperature. The color code denotes the normalized amplitude of the ΔFWHM response and blue corresponds to a predominantly CO-covered catalyst surface, whereas yellow denotes the O-covered state of the catalyst particle. Particle numbers shown on the upper right of each panel indicate the relative particle position along the model pore, where particle P1 is located most upstream, i.e., toward the inlet (see also Figure 6a).

kinetic phase transition downstream takes place at a higher nominal α^{CO}.

These trends can be rationalized in the following way. In the lower temperature regime, the turnover is relatively low, and since we, in contrast to our study of a single-particle Cu catalyst,[21] operate the system with both CO and O_2 in excess, no significant concentration gradients are created along the model pore due to reactant conversion. The slight negative position dependence of α^* is most likely rather the consequence of two factors: (i) the small pressure gradient along the pore (Figure S4) and (ii) the previously discussed structure-related single-particle-specific response. At the highest temperatures, this effect is then overcompensated by the appearance of significant gradients along the model pore due to the (now high) conversion on the catalyst, which changes the local α^{CO}. These results thus corroborate the main conclusion in our previous study of CO oxidation on single Cu nanoparticles[21] and emphasize the importance of understanding the local reaction conditions at the level of the individual nanoparticle inside the catalyst bed if, for example, proper structure−function relationships are to be derived and if severe ensemble averaging is to be avoided.

Unraveling Single-Catalyst Particle Surface Chemistry by Plasmonic Nanospectroscopy. To translate the measured optical response from the single nanoparticles into specific chemical information about the surface state of the catalyst nanoparticle, we first note that from the experiments, it is clear that the optical response is related to the presence of oxygen (Figures 1g, 4c,d, and S8), in agreement with previous studies on similar catalyst structures.[20,25] Based on this observation, we propose two processes that, in principle, could be responsible for the observed optical response: (i) Pt particle surface reconstruction and/or oxide formation and reduction[12,17] or (ii) spillover of dissociated O species from the Pt to the supporting SiO_2 layer, resulting in oxygen storage[32] and a change in the optical properties of the SiO_2 separating layer.[33−36] We believe that scenario (ii) is plausible because SiO_2 films grown by electron beam evaporation typically are oxygen deficient and amorphous[37] and can therefore take up and release oxygen. As we discuss below, this scenario is helpful to explain our experimental observations. However, we also note that we a priori do not have direct experimental evidence that this process occurs in our system

https://dx.doi.org/10.1021/acscatal.0c04955
ACS Catal. 2021, 11, 2021−2033

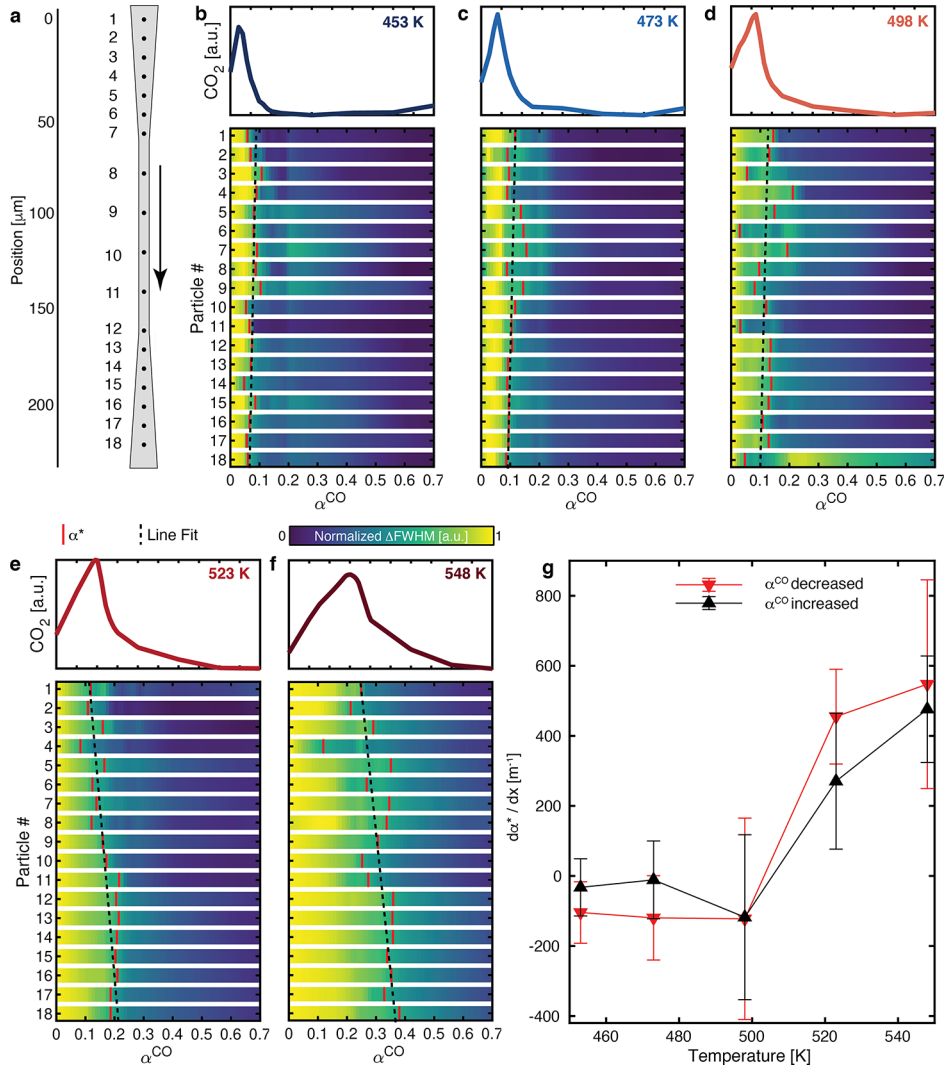

Figure 6. Single nanoparticle position dependence of the kinetic phase transition. (a) Schematic of the nanofluidic model pore with the 18 particles labeled with numbers (same as Figure 5). The arrow indicates the flow direction. (b–f) CO_2 production obtained from the QMS (top panels) and optical ΔFWHM response for the 18 particles (bottom panels) measured at five temperatures for an α^{CO} down sweep from 1 to 0. Corresponding data for an α^{CO} up sweep from 0 to 1 are presented in Figure S11. The ΔFWHM signal of each individual particle has been normalized. The solid red lines indicate the position of the kinetic phase transition at α^* extracted for each particle. The dashed black lines correspond to a linear regression of the single-particle α^*–values along the model pore. (g) Slope of the linear regression curves in (b)–(f) as a function of temperature for an α^{CO} up sweep and down sweep. The error bars correspond to 95% confidence intervals of the linear regression.

and it can also not be excluded that the process is more complicated due to the strong Si–O bond.

To deconvolute these potential contributions to the experimentally observed single-particle optical response, we utilized electrodynamics simulations to predict the optical response for different mechanisms. Specifically, we constructed a model using finite-difference time-domain (FDTD) simulations of the Au–SiO_2–Pt hybrid nanoarchitecture used in the experiments (see Figure 7a and Methods section for details). In the model, the hybrid nanostructure is represented by a Au truncated cone (D = 100 nm, H = 50 nm) and a Pt catalyst particle (disk shaped, D = 60 nm, H = 20 nm, with rounded edges), separated by an 8.5 nm thick SiO_2 layer. Here, we note that the exact dimensions of the Au and Pt components in the model were slightly tuned to match the experimentally measured spectral position of the scattering peak. The nanostructure is placed on a SiO_2 substrate and the scattering spectrum is collected by a power monitor placed above it (details in the Methods section). Using this model, we then simulate the two mechanisms proposed above as follows: (i) oxidizing a thin layer of the Pt nanoparticle surface by changing the dielectric function of a thin layer at the surface from metallic Pt to PtO_x[12,38] and (ii) increasing the refractive index (RI) of the SiO_2 to mimic a change in its dielectric properties due to addition of O species via spillover from the Pt catalyst.[39,40] We note that, since we do not know the exact optical properties of a Pt oxide formed in our case, we utilize the dielectric function of $PtO_{1.7}$ from the literature[41] for our simulations. To confirm that this uncertainty in the definition of the oxide dielectric function does not compromise our analysis, we have carried out additional FDTD simulations by varying the dielectric function of a 0.5 nm thick PtO_x layer over a range of $0.85 < x < 1.85$, which indeed resulted in negligible change of the peak FWHM and only a very small spectral shift of the peak maximum, on the order of 0.4 nm (Figure S12). Furthermore, we refer to the calculated value as an effective

https://dx.doi.org/10.1021/acscatal.0c04955
ACS Catal. 2021, 11, 2021–2033

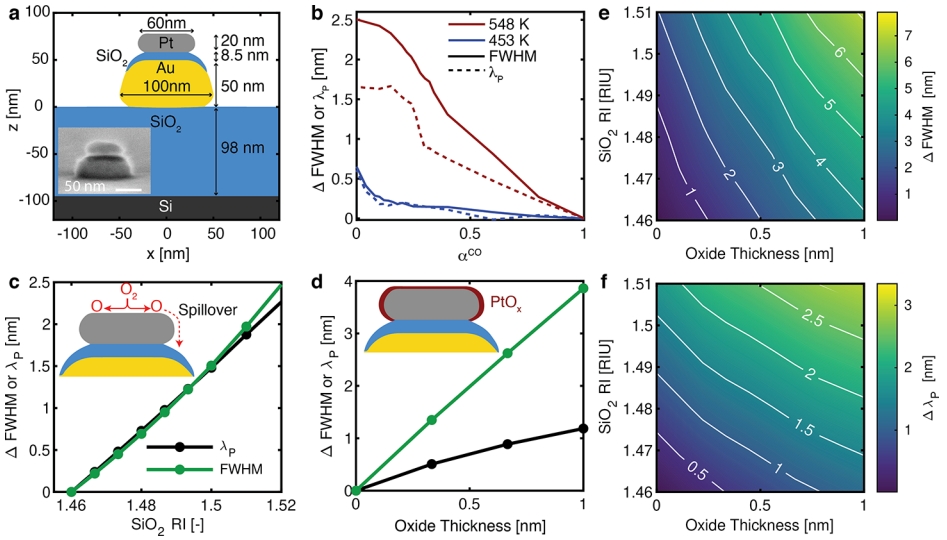

Figure 7. FDTD simulations. (a) Structural model used for FDTD simulations of the Au/SiO_2/Pt nanoparticle placed on a SiO_2/Si substrate. The inset shows the side-view SEM image of a representative nanostructure used in the experiments. (b) Experimentally measured change in FWHM and peak position (λ_P) during a sweep from high to low α^{CO} at 548 and 453 K. Note the absence (presence) of a difference between the FWHM and λ_P response at low (high) temperatures. Extended data set for all particles and temperatures in Figure S13. (c) $\Delta\lambda_P$ and ΔFWHM of the simulated scattering peak as a function of the refractive index (RI) of the SiO_2 layer separating the Pt and Au. The inset shows a schematic illustration of O_2 dissociation on Pt and spillover of O to the underlying SiO_2. (d) $\Delta\lambda_P$ and ΔFWHM of the simulated scattering peak as a function of the effective Pt-oxide thickness formed on the top Pt particle. The inset shows a schematic illustration of Pt-oxide (red) formation on the Pt. (e, f) Surface plot of the ΔFWHM (e) and $\Delta\lambda_P$ (f) response as a function of RI of SiO_2 (y-axis) and the Pt-oxide thickness (x-axis).

thickness since the model assumes the formation of a homogeneous layer and thus does not take potential local thickness variations (e.g., on different facets) into account.

Based on these simulations, we find that mechanisms (i) and (ii) in combination best reproduce the experimental single-particle response to an α^{CO} down sweep measured at 453 K and 548 K (Figure 7b; note that we now include both ΔFWHM and $\Delta\lambda_P$ in our analysis). Specifically, the FDTD model predicts that increasing the RI of SiO_2 results in an increase of both ΔFWHM and $\Delta\lambda_P$ and, as the key point, that they have the same magnitude (Figure 7c). In contrast, with the growth of a uniform oxide, the model predicts a relatively larger shift in ΔFWHM compared to the change in $\Delta\lambda_P$ (Figure 7d). Thus, as an intermediate conclusion, these simulations indicate that mostly an O spillover-induced change in the SiO_2 is responsible for the plasmonic nanospectroscopy response obtained at low temperatures, while the formation of a Pt-oxide layer becomes important at higher temperatures, where, in the experiment, we observe a significant difference in magnitude for ΔFWHM compared to $\Delta\lambda_P$ (compare Figure 7b–d).

In the next step of our analysis, we set out to use the FDTD simulations to extract quantitative information about the surface chemistry on the Pt nanoparticle across the α^{CO} sweeps at different temperatures. As a first step, by simulating the simultaneous occurrence of both a change in the RI of SiO_2 and the growth of a Pt oxide, we created two-dimensional (2D) surface representations of the corresponding optical signature (Figure 7e,f). It can be seen that indeed a combination of these two effects can create a response where ΔFWHM > $\Delta\lambda_P$, which is what is typically observed experimentally at higher temperatures (cf. Figures 7b and S13). In the next step, we thus fitted the simulated data with 2D polynomial functions with the form

$$\Delta\text{opt} = p_{00} + p_{10}x + p_{01}y + p_{20}x^2 + p_{11}xy + p_{02}y^2 \quad (2)$$

where Δopt is the optical response parameter (ΔFWHM or $\Delta\lambda_P$), p_{xx} are the parameters determined by the fit, and x and y are the RI of SiO_2 and the PtO_x thickness, respectively. The two polynomial functions describing ΔFWHM and $\Delta\lambda_P$ were then used to find the unique combination of effective Pt-oxide thickness and RI of SiO_2 that best reproduced the experimentally measured values. Specifically, this was done by minimizing the error function

$$\text{error}(x, y) = (\Delta\text{FWHM}_{\text{exp}} - \Delta\text{FWHM}(x, y))^2 + (\Delta\lambda_{P,\text{exp}} - \Delta\lambda_P(x, y))^2 \quad (3)$$

for each experimentally measured α^{CO} point. Here, the subscript exp corresponds to an experimental data point and ΔFWHM(x,y) and $\Delta\lambda(x,y)$ correspond to the values predicted by the polynomial equations described by eq 2. The simulated ΔFWHM and $\Delta\lambda_P$ obtained by this fitting procedure are presented in Figure 8a together with the experimental values for each temperature during sweeps from high to low α^{CO}. Evidently, the experimental results can be very accurately reproduced by assuming a surface chemistry where the dominant and simultaneously occurring processes are the spillover of dissociated O from the Pt particle to the SiO_2 layer, and the formation of a PtO_x layer at higher temperatures (Figure 8a).

Consequently, we can now use the fitted data to produce SiO_2 RI change and Pt-oxide effective thickness trajectories along the experimental α^{CO} sweeps at the five measured temperatures to quantitatively extract the evolution of these two parameters as a function of α^{CO} from the experiment for single nanoparticles. Such trajectories are presented as individual points for each experimental α^{CO} step in the 2D surface plots in Figure 8b for the same particle also

https://dx.doi.org/10.1021/acscatal.0c04955
ACS Catal. 2021, 11, 2021−2033

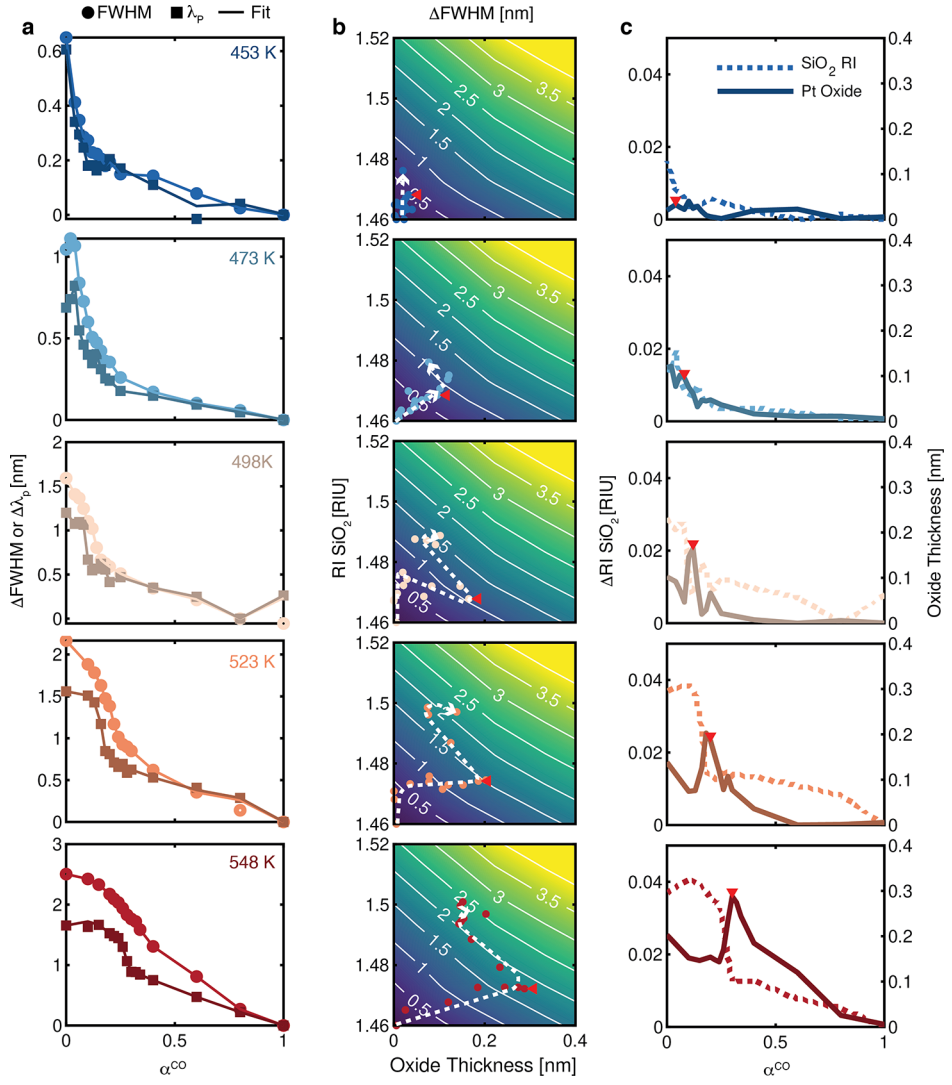

Figure 8. Unraveling single-catalyst particle surface chemistry with FDTD simulations. (a) Experimental (symbols) and fitted parameters (lines) for a sweep from high to low α^{CO} values. (b) Two-dimensional surface plots of the change in FWHM (same as Figure 7e), with the corresponding fitted experimental points presented as color-coded circles. The white lines serve as a guide for the eye. Corresponding data for $\Delta\lambda$ are presented in Figure S15. (c) Change in RI of SiO_2 and Pt-oxide thickness found by fitting each experimental point to the model presented in Figure 5. Red triangles in (b, c) indicate the location of the maximum CO_2 production measured by the QMS.

characterized in Figure 4. The white dashed line serves as a guide to the eye and indicates the direction of the trajectory. The corresponding absolute values of the SiO_2 refractive index and PtO_x effective thickness found by the fitting procedure at each point of the α^{CO} sweep are presented in Figure 8c as a function of α^{CO}. As the main observations, we see that oxide formation is more pronounced at higher reaction temperatures and that the catalyst surface, at high temperatures, is oxidized at the point where the maximum CO_2 production is measured by the QMS.

For reference, it is important to note that the unique nature of each nanoparticle results in quantitatively slightly different optical responses of the individuals (Figures S9 and S13). As a consequence, the use of a single model to describe all particles will result in quantitatively slightly different results for each particle. Therefore, comparing absolute numbers in terms of effective oxide thickness between particles is not meaningful here and we focus on a qualitative comparison. Accordingly, performing the same analysis for additional single particles reveals a similar trend with respect to increasing spillover and Pt-oxide formation for elevated reaction temperatures, but also differences at the individual level (Figure S14). We argue that these differences partially are related to single-particle-specific morphology and partly the consequence of somewhat different optical response amplitudes at the individual level, dictated by the exact relative positions of the components in the $Au/SiO_2/Pt$ architecture.[42]

From our analysis, we can draw a number of intermediate conclusions. First, we note that at the lowest temperature (453 K), no significant PtO_x formation is observed. In other words, the main contribution to the optical response is a change in the RI of the SiO_2 layer due to spillover of dissociated O from the Pt catalyst. As we then increase the temperature, we start to observe the formation of a surface oxide, which increases in effective thickness up to ca. 0.3 nm at the highest measured temperature, 548 K. Simultaneously, with increased temperature, we also detect a higher degree of change in the SiO_2 layer. This can be explained by considering that O first has to spill over from Pt to the SiO_2, followed by diffusion through the SiO_2.[43] Hence, the rate of spillover can be assumed to

https://dx.doi.org/10.1021/acscatal.0c04955
ACS Catal. 2021, 11, 2021−2033

depend on the O coverage on the Pt, which in turn is inversely proportional to the CO coverage. Since at higher temperatures the CO desorption rate increases, more sites become available for O_2 dissociation and the resulting available O species can participate in both CO oxidation at a higher rate and in the spillover to the SiO_2. Finally, the data also show that at high temperatures, a Pt surface oxide is formed in the regime of high catalyst activity, in agreement with previous studies identifying a surface oxide as the active phase under similar conditions.[8,9]

CONCLUSIONS

We have demonstrated how single-particle plasmonic nanospectroscopy in combination with a nanofluidic reactor can be used to investigate the surface state dynamics of a small population of individual Pt catalyst nanoparticles in the 70 nm × 20 nm size range. In situ experiments were conducted during the CO oxidation reaction at 453−548 K and the confinement imposed by the nanochannels served to mimic the conditions inside a porous support material. Using this concept, we identified single-particle-specific kinetic phase transitions from a CO-dominated surface state to an O-dominated surface state and the corresponding kinetic bistability in the low-temperature regime. As the origin of the particle-specific behavior, we identified the nanoparticle morphology, which is characterized by the particles' polycrystalline nature and the corresponding particle-specific abundance of grain boundaries and exposed surface facets. Direct correlation with the CO_2 formation rate measured simultaneously using a QMS from an ensemble of ca. 3×10^4 nanoparticles of identical size present on the same nanoreactor chip revealed the highest catalyst activity at the reactant mixture where the kinetic phase transition occurred. At higher temperatures, where kinetic bistability was absent, we observed reactant concentration gradient formation along the model pore due to conversion on the single nanoparticles, which manifested itself as position-dependent kinetic phase transitions along the model pore. Finally, using extensive electrodynamics simulations paired with corresponding experiments, we characterized the surface chemistry of the individual Pt nanoparticles as a function of reactant composition and temperature. As the main results, we found temperature-dependent Pt-oxide formation and oxygen spillover to the SiO_2 support, where both the amount of oxygen stored in the SiO_2 and the thickness of the formed Pt oxide increased with temperature. Since a surface oxide was observed at the state of the highest catalyst activity, our findings indicate, at the single nanoparticle level, that a (partially) oxidized surface is present during high activity under high pressure and temperature conditions.[8,9] This is in line with the recent theoretical prediction[14] that partially oxide-covered surfaces can exhibit essentially the same turnover frequency up to 80% coverage, and it may imply that the highest activity occurs at the interface between the oxidized and the metallic surface.

In a broader context, this study thus highlights the potential of single-particle plasmonic nanospectroscopy as an in situ probe of the surface state of catalyst particles and how correlated detailed electrodynamics simulations enable the semiquantitative interpretation of the single nanoparticle data. At the same time, we acknowledge that the model catalyst particles studied here are approximately 1 order of magnitude larger than particles used in commercial catalysts. Nevertheless, we propose that similar single-particle morphology and spatial position-dependent effects are likely to exist also for smaller nanoparticles and highlight the importance of studying catalysts on several length scales. Looking forward, we thus also suggest the further use and development of antenna-enhanced plasmonic nanospectroscopy solutions to enable the study of single nanoparticles in the sub-50 nm size range.[42,44,45] Also, alternative solutions, such as photothermal imaging or interferometric scattering microscopy, may become important since they have the potential to enable the in situ characterization of even smaller catalyst nanoparticles.[46,47] Furthermore, we envision combinations of plasmonic nanospectroscopy on open sample surfaces with other in situ techniques, such as ambient-pressure TEM[18,19] and nano-IR, to enable more direct correlations between nanoparticle structure, chemistry, and plasmonic response, as already demonstrated in a study of single Cu nanoparticle oxidation[48] or hydride formation in single Pd nanoparticles.[22] Finally, we highlight that single-particle plasmonic nanoimaging can be used to investigate large numbers of individual nanoparticles in parallel, which makes optical characterization of the whole catalyst bed possible, while activity measurements from the same bed become readily available in combination with nanofluidic reactors.[27] Therefore, we propose the development of transmission electron microscopy-compatible nanoreactors to enable measurements of single-particle structure−function correlations within a catalyst bed that is large enough to enable statistical analysis of hundreds to thousands of individual particles measured simultaneously, to thereby minimize measurement-to-measurement artifacts and ensure that the averaged single-particle response reproduces the response of the whole catalyst bed.

METHODS

Nanofabrication of Nanoreactor Chips. The reactor chips were fabricated in cleanroom facilities of Fed. Std.209E Class 10−100 following a number of steps including lithography (electron beam and optical), chemical (wet) etching, and reactive ion etching (RIE), and deposition of material via electron beam evaporation. The main nanofabrication steps are illustrated in Figure S2 in the Supporting Information. Details of the fabrication steps of the chips are presented in our previous work and the same recipe was used here also.[18,19] The catalyst nanoparticles were made by evaporating 40 nm Au, 7 nm SiO_2, and 15 nm Pt through an evaporation mask made by electron beam lithography.

Optical Data Acquisition and Analysis. The optical readout was performed with a spectrometer (Andor Kymera 193i) and an EM-CCD camera (iXon Ultra 888) connected to a Nikon LV150 microscope with a Nikon LU Plan ELWD 50 X/0.55objective. For spectroscopic measurements, a grating with 150 lines/mm, 630 nm central wavelength, and an integration time of 0.5 s were used. Spectra of several individual nanoparticles were collected using the multitrack option in Andor Solis software and integrating the light from a region 5 to 10 pixel rows above and below each particle of interest. Background subtraction was done for each particle individually by taking a spectrum below each nanoparticle. The final signal was calculated as $I(\lambda) = (S-B)/CRS$, where S is the raw signal measured from a region with a particle, B is the background signal, and CRS is the spectrum of the 50 W halogen lamp collected from a certified diffuse white reflectance standard reference sample (Labsphere SRS-99-020).

The peak characteristics (FWHM and λ_P) were found by fitting a polynomial function (16°) to the corrected scattering

https://dx.doi.org/10.1021/acscatal.0c04955
ACS Catal. 2021, 11, 2021−2033

spectra and finding the maximum point and the full width at half of the maximum of the polynomial. In figures where the change in an optical parameter (e.g., ΔFWHM) was used, each data point was calculated by subtracting the first value in the series, i.e., $\Delta\mathrm{FWHM}(x) = \mathrm{FWHM}(x) - \mathrm{FWHM}(1)$, where x is either the time or the relevant α^{CO} step. Normalized optical responses, as used in Figures 5 and 6, were created by dividing the change in the optical response with the maximum shift in the interval.

Experimental Details. For the CO oxidation experiments, ultrapure CO (10% in Ar) and O_2 (2% in Ar) were used with Ar carrier gas (99.99999% purity) and fed with different concentrations into the chip. The inlet pressure was set to 4 bar, and a total flow of 10 mL/min through the microchannels was applied.

RHEED Characterization. The RHEED investigation was performed in a UHV system using 25 keV electron energy at incidence angles in a range of 0.5−1° to the surface. A CCD camera recorded the diffraction patterns appearing on a phosphor screen. A total of 200 single RHEED images were acquired and averaged to greatly improve the signal-to-noise ratio. The well-known Si(111)7 × 7 surface[49] served as a reference to calculate atomic distances in the RHEED image.

TEM Characterization. The analogue Pt nanoparticles were prepared on SiNx TEM membranes and annealed at 823 K and imaged with an FEI Titan 80−300 (FEG filament operated at 300 kV). Imaging was done in bright-field mode at 145−790k× magnification.

FDTD Simulations. Finite-difference time-domain (FDTD) simulations, performed using the commercial software FDTD Solutions (Lumerical), were used to evaluate the optical response of the plasmonic nanostructures. A schematic figure of a structure used in the simulation is presented in Figure 7, where the substrate was simulated as SiO_2 with a Si layer placed 98 nm below the surface. The particle of interest was placed on the SiO_2, and the dimensions of the particle of interest are specified in Figure 5 and the corresponding text. SiO_2 was simulated as a material with a dielectric function taken from Palik[50] or as a constant refractive index when specified. The Au dielectric function was taken from Johnson and Christy,[51] the one for Pt from Palik,[50] and the one for Pt oxide from Li et al.[41] for an oxide with stoichiometry $PtO_{1.7}$. To correctly resolve the field close to the Pt nanoparticle, a mesh overlay with a step size of 0.3 nm was used around it. Light was introduced as a linearly polarized plane wave via a total-field/scattered-field source and the backward scattering was collected by integrating the Poynting vector of the field in the backward direction with respect to the incident light, using an area corresponding to the numerical aperture of the microscope objective used in the experiment (NA = 0.55).

The growth of an oxide layer on the Pt particle was simulated as an oxide growing from the surface toward the center of the Pt particle. The volume expansion (Pilling−Bedworth ratio) of the oxide was assumed to be the same as that for a PtO structure, resulting in a volume expansion factor of 1.56.

■ ASSOCIATED CONTENT

Supporting Information

The Supporting Information is available free of charge at https://pubs.acs.org/doi/10.1021/acscatal.0c04955.

Schematic of the experimental setup; schematic of the nanofluidic chip; fabrication process of the nanofluidic chip; pressure profiles; additional experimental data; and alternative representation of optical data (PDF)

■ AUTHOR INFORMATION

Corresponding Author

Christoph Langhammer − *Department of Physics, Chalmers University of Technology, 412 96 Göteborg, Sweden;* orcid.org/0000-0003-2180-1379; Email: clangham@chalmers.se

Authors

David Albinsson − *Department of Physics, Chalmers University of Technology, 412 96 Göteborg, Sweden;* orcid.org/0000-0001-7275-6921

Stephan Bartling − *Department of Physics, Chalmers University of Technology, 412 96 Göteborg, Sweden;* orcid.org/0000-0001-5901-7235

Sara Nilsson − *Department of Physics, Chalmers University of Technology, 412 96 Göteborg, Sweden*

Henrik Ström − *Department of Mechanics and Maritime Sciences, Chalmers University of Technology, 412 96 Göteborg, Sweden; Department of Energy and Process Engineering, Norwegian University of Science and Technology, 7491 Trondheim, Norway;* orcid.org/0000-0002-8581-5174

Joachim Fritzsche − *Department of Physics, Chalmers University of Technology, 412 96 Göteborg, Sweden*

Complete contact information is available at: https://pubs.acs.org/10.1021/acscatal.0c04955

Author Contributions

The manuscript was written through contributions of all authors. All authors have given approval to the final version of the manuscript.

Notes

The authors declare no competing financial interest.

■ ACKNOWLEDGMENTS

This research received funding from the European Research Council (ERC) under the European Union's Horizon 2020 research and innovation program (678941/SINCAT) and from the Knut and Alice Wallenberg Foundation project 2015.0055. Part of this work was carried out at the MC2 cleanroom facility and at the Chalmers Materials Analysis Laboratory. S.B. thanks the group of Prof. S. Speller and I. Barke at the University of Rostock, Institute for Physics, for use of the RHEED setup.

■ REFERENCES

(1) Imbihl, R.; Ertl, G. Oscillatory Kinetics in Heterogeneous Catalysis. *Chem. Rev.* **1995**, *95*, 697−733.

(2) Vendelbo, S. B.; Elkjær, C. F.; Falsig, H.; Puspitasari, I.; Dona, P.; Mele, L.; Morana, B.; Nelissen, B. J.; Van Rijn, R.; Creemer, J. F.; Kooyman, P. J.; Helveg, S. Visualization of Oscillatory Behaviour of Pt Nanoparticles Catalysing CO Oxidation. *Nat. Mater.* **2014**, *13*, 884−890.

(3) Vogel, D.; Spiel, C.; Suchorski, Y.; Trinchero, A.; Schlögl, R.; Grönbeck, H.; Rupprechter, G. Local Catalytic Ignition during CO Oxidation on Low-Index Pt and Pd Surfaces: A Combined PEEM, MS, and DFT Study. *Angew. Chem., Int. Ed.* **2012**, *51*, 10041−10044.

(4) Krick Calderón, S.; Grabau, M.; Óvári, L.; Kress, B.; Steinrück, H.-P.; Papp, C. CO Oxidation on Pt(111) at near Ambient Pressures. *J. Chem. Phys.* **2016**, *144*, No. 044706.
(5) Johanek, V.; Johánek, V.; Laurin, M.; Grant, A. W.; Kasemo, B.; Henry, C. R.; Libuda, J. Fluctuations and Bistabilities on Catalyst Nanoparticles. *Science* **2004**, *304*, 1639−1644.
(6) Wang, H.; Shen, T.; Duan, S.; Chen, Z.; Xu, X. Bistability for CO Oxidation: An Understanding from Extended Phenomenological Kinetics Simulations. *ACS Catal.* **2019**, *9*, 11116−11124.
(7) Zhdanov, V. P.; Kasemo, B. Kinetic Phase Transitions in Simple Reactions on Solid Surfaces. *Surf. Sci. Rep.* **1994**, *20*, 113−189.
(8) Ackermann, M. D.; Pedersen, T. M.; Hendriksen, B. L. M.; Robach, O.; Bobaru, S. C.; Popa, I.; Quiros, C.; Kim, H.; Hammer, B.; Ferrer, S.; Frenken, J. W. M. Structure and Reactivity of Surface Oxides on Pt(110) during Catalytic CO Oxidation. *Phys. Rev. Lett.* **2005**, *95*, No. 255505.
(9) Singh, J.; Nachtegaal, M.; Alayon, E. M. C.; Stötzel, J.; van Bokhoven, J. A. Dynamic Structure Changes of a Heterogeneous Catalyst within a Reactor: Oscillations in CO Oxidation over a Supported Platinum Catalyst. *ChemCatChem* **2010**, *2*, 653−657.
(10) Gänzler, A. M.; Casapu, M.; Boubnov, A.; Müller, O.; Conrad, S.; Lichtenberg, H.; Frahm, R.; Grunwaldt, J.-D. Operando Spatially and Time-Resolved X-Ray Absorption Spectroscopy and Infrared Thermography during Oscillatory CO Oxidation. *J. Catal.* **2015**, *328*, 216−224.
(11) Yu, Y.; Koh, Y. E.; Lim, H.; Jeong, B.; Isegawa, K.; Kim, D.; Ueda, K.; Kondoh, H.; Mase, K.; Crumlin, E. J.; Ross, P. N.; Gallet, J.-J.; Bournel, F.; Mun, B. S. Chemical States of Surface Oxygen during CO Oxidation on Pt(1 1 0) Surface Revealed by Ambient Pressure XPS. *J. Phys.: Condens. Matter* **2017**, *29*, No. 464001.
(12) Newton, M. Time Resolved Operando X-Ray Techniques in Catalysis, a Case Study: CO Oxidation by O_2 over Pt Surfaces and Alumina Supported Pt Catalysts. *Catalysts* **2017**, *7*, 58.
(13) Gao, F.; Wang, Y.; Cai, Y.; W. Goodman, D. CO Oxidation on Pt-Group Metals from Ultrahigh Vacuum to Near Atmospheric Pressures. 2. Palladium and Platinum. *J. Phys. Chem. C* **2008**, *113*, 174−181.
(14) Makeev, A. G.; Slinko, M. M.; Luss, D. Mathematical Modeling of Oscillating CO Oxidation on Pt-Group Metals at near Atmospheric Pressure: Activity of Metallic and Oxidized Surfaces. *Appl. Catal., A* **2019**, *571*, 127−136.
(15) Ertl, G. Reactions at Well-Defined Surfaces. *Surf. Sci.* **1994**, *299*−*300*, 742−754.
(16) Vogel, D.; Spiel, C.; Schmid, M.; Stöger-Pollach, M.; Schlögl, R.; Suchorski, Y.; Rupprechter, G. The Role of Defects in the Local Reaction Kinetics of CO Oxidation on Low-Index Pd Surfaces. *J. Phys. Chem. C* **2013**, *117*, 12054−12060.
(17) van Spronsen, M. A.; Frenken, J. W. M.; Groot, I. M. N. Surface Science under Reaction Conditions: CO Oxidation on Pt and Pd Model Catalysts. *Chem. Soc. Rev.* **2017**, *46*, 4347−4374.
(18) Chee, S. W.; Arce-Ramos, J. M.; Li, W.; Genest, A.; Mirsaidov, U. Structural Changes in Noble Metal Nanoparticles during CO Oxidation and Their Impact on Catalyst Activity. *Nat. Commun.* **2020**, *11*, No. 2133.
(19) Plodinec, M.; Nerl, H. C.; Girgsdies, F.; Schlögl, R.; Lunkenbein, T. Insights into Chemical Dynamics and Their Impact on the Reactivity of Pt Nanoparticles during CO Oxidation by Operando TEM. *ACS Catal.* **2020**, *10*, 3183−3193.
(20) Liu, S.; Susarrey-Arce, A.; Nilsson, S.; Albinsson, D.; Hellberg, L.; Alekseeva, S.; Langhammer, C.; Susarrey Arce, A.; Nilsson, S.; Albinsson, D.; Hellberg, L.; Alekseeva, S.; Langhammer, C. In Situ Plasmonic Nanospectroscopy of the CO Oxidation Reaction over Single Pt Nanoparticles. *ACS Nano* **2019**, *13*, 6090−6100.
(21) Albinsson, D.; Bartling, S.; Nilsson, S.; Ström, H.; Fritzsche, J.; Langhammer, C. Operando Detection of Single Nanoparticle Activity Dynamics inside a Model Pore Catalyst Material. *Sci. Adv.* **2020**, *6*, No. eaba7678.
(22) Alekseeva, S.; Fanta, A. B.; da, S.; Iandolo, B.; Antosiewicz, T. J.; Nugroho, F. A. A.; Wagner, J. B.; Burrows, A.; Zhdanov, V. P.; Langhammer, C. Grain Boundary Mediated Hydriding Phase Transformations in Individual Polycrystalline Metal Nanoparticles. *Nat. Commun.* **2017**, *8*, No. 1084.
(23) Garcia, M. A. Surface Plasmons in Metallic Nanoparticles: Fundamentals and Applications. *J. Phys. D: Appl. Phys.* **2011**, *44*, No. 283001.
(24) Willets, K. A.; Van Duyne, R. P. Localized Surface Plasmon Resonance Spectroscopy and Sensing. *Annu. Rev. Phys. Chem.* **2007**, *58*, 267−297.
(25) Larsson, E. M.; Langhammer, C.; Zoric, I.; Kasemo, B. Nanoplasmonic Probes of Catalytic Reactions. *Science* **2009**, *326*, 1091−1094.
(26) Alekseeva, S.; Nedrygailov, I. I.; Langhammer, C. Single Particle Plasmonics for Materials Science and Single Particle Catalysis. *ACS Photonics* **2019**, *6*, 1319−1330.
(27) Albinsson, D.; Boje, A.; Nilsson, S.; Tiburski, C.; Hellman, A.; Ström, H.; Langhammer, C. Copper Catalysis at Operando Conditions—Bridging the Gap between Single Nanoparticle Probing and Catalyst-Bed-Averaging. *Nat. Commun.* **2020**, *11*, No. 4832.
(28) Taylor, A. B.; Zijlstra, P. Single-Molecule Plasmon Sensing: Current Status and Future Prospects. *ACS Sensors* **2017**, *2*, 1103−1122.
(29) Fritzsche, J.; Albinsson, D.; Fritzsche, M.; Antosiewicz, T. J.; Westerlund, F.; Langhammer, C. Single Particle Nanoplasmonic Sensing in Individual Nanofluidic Channels. *Nano Lett.* **2016**, *16*, 7857−7864.
(30) Engel, T.; Ertl, G. Oxidation of Carbon Monoxide. In *The Chemical Physics of Solid Surfaces and Heterogeneous Catalysis*; King, D. A., Ed.; Elsevier, 1982; pp 73−93.
(31) Jørgensen, M.; Grönbeck, H. The Site-Assembly Determines Catalytic Activity of Nanoparticles. *Angew. Chem., Int. Ed.* **2018**, *57*, 5086−5089.
(32) Ono, L. K.; Croy, J. R.; Heinrich, H.; Roldan Cuenya, B. Oxygen Chemisorption, Formation, and Thermal Stability of Pt Oxides on Pt Nanoparticles Supported on SiO_2/Si(001): Size Effects. *J. Phys. Chem. C* **2011**, *115*, 16856−16866.
(33) Schalwig, J.; Kreisl, P.; Ahlers, S.; Muller, G. Response Mechanism of SiC-Based MOS Field-Effect Gas Sensors. *IEEE Sens. J.* **2002**, *2*, 394−402.
(34) Ma, H.-P.; Yang, J.-H.; Yang, J.-G.; Zhu, L.-Y.; Huang, W.; Yuan, G.-J.; Feng, J.-J.; Jen, T.-C.; Lu, H.-L. Systematic Study of the SiO(x) Film with Different Stoichiometry by Plasma-Enhanced Atomic Layer Deposition and Its Application in SiO(x)/SiO_2 Super-Lattice. *Nanomaterials* **2019**, *9*, 55.
(35) Wallin, M.; Grönbeck, H.; Spetz, A. L.; Eriksson, M.; Skoglundh, M. Vibrational Analysis of H_2 and D_2 Adsorption on Pt/SiO_2. *J. Phys. Chem. B* **2005**, *109*, 9581−9588.
(36) Collins, S. S. E.; Cittadini, M.; Pecharromán, C.; Martucci, A.; Mulvaney, P. Hydrogen Spillover between Single Gold Nanorods and Metal Oxide Supports: A Surface Plasmon Spectroscopy Study. *ACS Nano* **2015**, *9*, 7846−7856.
(37) Baumann, S. M.; Martner, C. C.; Martin, D. W.; Blattner, R. J.; Braundmeier, A. J. A Study of Electron Beam Evaporated SiO2, TiO2, and Al2O2 Films Using RBS, HFS, and SIMS. *Nucl. Instrum. Methods Phys. Res., Sect. B* **1990**, *45*, 664−668.
(38) van Spronsen, M. A.; Frenken, J. W. M.; Groot, I. M. N. Observing the Oxidation of Platinum. *Nat. Commun.* **2017**, *8*, No. 429.
(39) Becker, E.; Andersson, M.; Eriksson, M.; Spetz, A. L.; Skoglundh, M. Study of the Sensing Mechanism Towards Carbon Monoxide of Platinum-Based Field Effect Sensors. *IEEE Sens. J.* **2011**, *11*, 1527−1534.
(40) Eriksson, M.; Petersson, L.-G. Spillover of Hydrogen, Oxygen and Carbon Monoxide in Oxidation Reactions on SiO2 Supported Pd. *Surf. Sci.* **1994**, *311*, 139−152.
(41) Li, X.; Kim, C. Il.; An, S. H.; Oh, S. G.; Kim, S. Y. Optical Property of PtO_x at Elevated Temperatures Investigated by Ellipsometry. *Jpn. J. Appl. Phys.* **2005**, *44*, 3623−3626.

https://dx.doi.org/10.1021/acscatal.0c04955
ACS Catal. 2021, 11, 2021−2033

(42) Syrenova, S.; Wadell, C.; Nugroho, F. A. A.; Gschneidtner, T. A.; Diaz Fernandez, Y. A.; Nalin, G.; Switlik, D.; Westerlund, F.; Antosiewicz, T. J.; Zhdanov, V. P.; Moth-Poulsen, K.; Langhammer, C. Hydride Formation Thermodynamics and Hysteresis in Individual Pd Nanocrystals with Different Size and Shape. *Nat. Mater.* **2015**, *14*, 1236−1244.
(43) Hoshino, T.; Hata, M.; Neya, S.; Nishioka, Y.; Watanabe, T.; Tatsumura, K.; Ohdomari, I. Diffusion of Molecular and Atomic Oxygen in Silicon Oxide. *Jpn. J. Appl. Phys.* **2003**, *42*, 3560−3565.
(44) Liu, N.; Tang, M. L.; Hentschel, M.; Giessen, H.; Alivisatos, A. P. Nanoantenna-Enhanced Gas Sensing in a Single Tailored Nanofocus. *Nat. Mater.* **2011**, *10*, 631−636.
(45) Syrenova, S.; Wadell, C.; Langhammer, C. Shrinking-Hole Colloidal Lithography: Self-Aligned Nanofabrication of Complex Plasmonic Nanoantennas. *Nano Lett.* **2014**, *14*, 2655−2663.
(46) Boyer, D.; Tamarat, P.; Maali, A.; Lounis, B.; Orrit, M. Photothermal Imaging of Nanometer-Sized Metal Particles among Scatterers. *Science* **2002**, *297*, 1160−1163.
(47) Young, G.; Hundt, N.; Cole, D.; Fineberg, A.; Andrecka, J.; Tyler, A.; Olerinyova, A.; Ansari, A.; Marklund, E. G.; Collier, M. P.; Chandler, S. A.; Tkachenko, O.; Allen, J.; Crispin, M.; Billington, N.; Takagi, Y.; Sellers, J. R.; Eichmann, C.; Selenko, P.; Frey, L.; Riek, R.; Galpin, M. R.; Struwe, W. B.; Benesch, J. L. P.; Kukura, P. Quantitative Mass Imaging of Single Biological Macromolecules. *Science* **2018**, *360*, 423−427.
(48) Nilsson, S.; Albinsson, D.; Antosiewicz, T. J.; Fritzsche, J.; Langhammer, C. Resolving Single Cu Nanoparticle Oxidation and Kirkendall Void Formation with in Situ Plasmonic Nanospectroscopy and Electrodynamic Simulations. *Nanoscale* **2019**, *11*, 20725−20733.
(49) Mahan, J. E.; Geib, K. M.; Robinson, G. Y.; Long, R. G. A Review of the Geometrical Fundamentals of Reflection High-energy Electron Diffraction with Application to Silicon Surfaces. *J. Vac. Sci. Technol., A* **1990**, *8*, 3692−3700.
(50) Palik, E. D. *Handbook of Optical Constants of Solids*; Academic Press, 1985; Vol. *1*, pp 1−804.
(51) Johnson, P. B.; Christy, R. W. Optical Constants of the Noble Metals. *Phys. Rev. B* **1972**, *6*, 4370−4379.

https://dx.doi.org/10.1021/acscatal.0c04955
ACS Catal. 2021, 11, 2021−2033